Life Science

The year 2025 marks a significant leap in integrative structural biology. While synchrotron macromolecular crystallography remains the cornerstone for determining atomic-resolution structures, the field is increasingly enriched by complementary techniques such as AI-based modeling, cryogenic electron microscopy (cryo-EM), and microcrystal electron diffraction (MicroED). This synergistic approach enables researchers to visualize static architectures and decipher dynamic conformational changes and complex enzymatic mechanisms essential for survival and disease progression.

The NSRRC remains a pivotal hub for advanced life science research. The core protein crystallography beamlines (**TLS 15A1**, **TPS 05A**, and **TPS 07A**) provide high-intensity X-rays essential for resolving novel enzyme structures and drug targets. Following the upgrade program initiated last year, **TPS 05A** and **TPS 07A** are improving their automation and micro-crystallography capabilities. Beyond crystallography, the use of specialized beamlines has increased: biological small-angle X-ray scattering (**TPS 13A**) is increasingly used to monitor structural remodeling in solution; soft X-ray tomography (**TPS 24A**) offers high-resolution 3D cellular imaging for biomedical applications; and infrared microspectroscopy (**TLS 14A1**) is advancing label-free clinical diagnostics. Together, these facilities support a broad spectrum of research, from fundamental biochemistry to translational medicine.

In 2025, our user community achieved significant breakthroughs, with six outstanding reports selected for this activity report. Hanna S. Yuan revealed how histone marks activate the DNA-methylation enzyme DNMT3B through structural remodeling. The Maestre-Reyna and Essen teams used serial femtosecond crystallography to reveal undistorted cofactor structures, uncovering energy conversion mechanisms. Jiashing Yu and Ken-Tsung Wong developed nanocomposites with superior near-infrared photothermal and photodynamic therapeutic effects. A joint team from National Tsing Hua University and National Chung Hsing University identified *Staphylococcus aureus* (ScdA) as a nitric oxide-generating reductase involved in stress resistance. Rey-Ting Guo defined a distinct class of terpenoid cyclases with unique metal coordination for abscisic acid biosynthesis. Finally, Mei-Ching Yu and Yao-Chang Lee developed a label-free infrared spectroscopy technique to track lupus nephritis activity using serum biochemical fingerprints. (by Chun-Hsiang Huang)

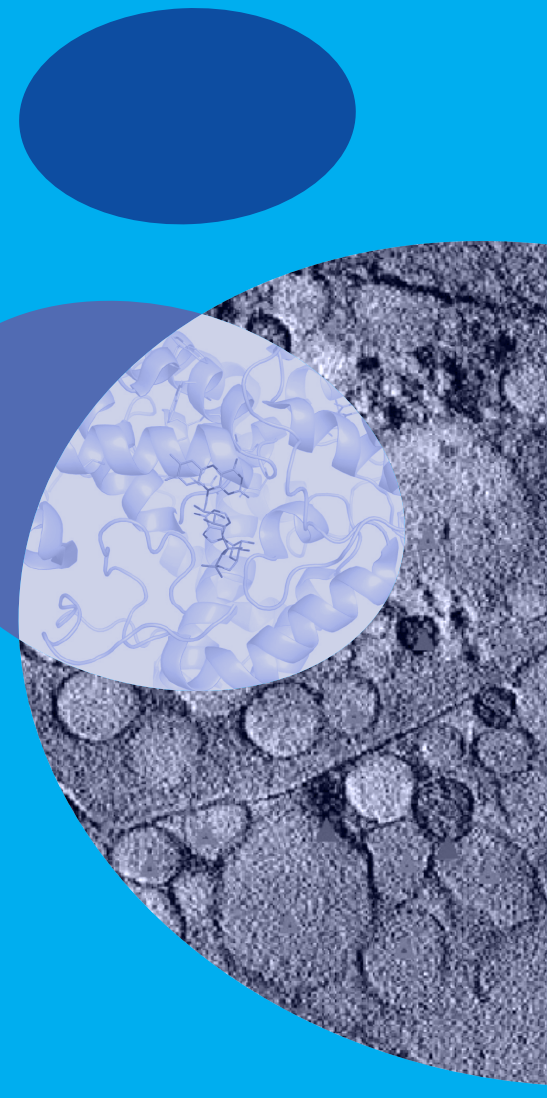

How Histone Marks Activate a Key DNA-Methylation Enzyme

New research shows how specific histone marks reshape and activate DNMT3B, revealing a long-sought mechanism that links chromatin signals to gene-silencing pathways.

Our genes are packaged in a complex structure called chromatin, where proteins known as histones help control which genes are active or silent. Another layer of control is DNA methylation—chemical tags added directly to DNA that can turn genes off (**Fig. 1**). For years, scientists have known that histone marks and DNA methylation interact, but the mechanism underlying this crosstalk has remained unclear.

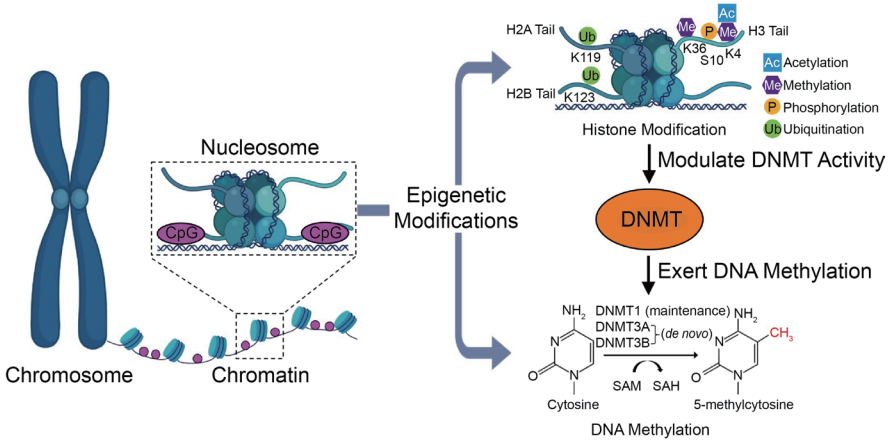

Fig. 1: Schematic representation of the interplay between DNA methylation and histone modifications at nucleosomes. CpG dinucleotides within nucleosomal DNA are methylated at the C5 position of cytosine through transfer of a methyl group from S-adenosylmethionine (SAM), catalyzed by DNA methyltransferases (DNMTs), including DNMT1, DNMT3A, and DNMT3B. Core histones (H2A, H2B, H3, and H4) undergo various post-translational modifications, such as ubiquitination, acetylation, methylation, and phosphorylation. The catalytic activity of DNMT3B is regulated by specific histone marks, notably unmethylated H3K4 and trimethylated H3K36.

A recent study published in *Science Advances* by Hanna S. Yuan's team (Academia Sinica) uncovers a major piece of this puzzle.[1] The researchers investigated DNMT3B, an enzyme responsible for adding new methylation marks to DNA. DNMT3B is essential during early embryonic development and is also misregulated in several diseases, including cancer.[2,3]

Yuan's team discovered that a histone H3 peptide containing unmethylated H3K4 and methylated H3K36 markedly enhances the enzymatic activity and DNA-binding capacity of DNMT3B (**Fig. 2(a)**, see next page). In addition, using the X-ray protein crystallography facilities at beamlines **TLS 15A1** and **TPS 05A**, the team determined the structure of the PWWP domain of human DNMT3B. Their structural analysis showed that differences in the orientations of lysine side chains on the protein surface generate a more positively charged surface potential when the PWWP domain binds the histone H3 tail with a tri-methylated K36 residue (**Figs. 2(b) and 2(c)**), thereby explaining how histone modifications modulate DNMT3B activity by facilitating PWWP-mediated DNA binding.

Using the small-angle X-ray scattering (SAXS) facility at the beamline **TPS 13A**, Yuan's team discovered that DNMT3B does not passively await DNA binding. Instead, it is typically maintained in an inactive conformation, in which the ADD domain interacts with the catalytic domain and occludes the DNA-binding site. Specific histone modifications—particularly the combination of unmethylated H3K4 and methylated H3K36—serve as a molecular key that unlocks and reconfigures DNMT3B. In the presence of these histone signals, DNMT3B undergoes a substantial structural rearrangement: the ADD domain shifts to a position beneath the catalytic domain, while the PWWP domain moves into closer alignment with it, fully activating the enzyme and enabling DNA methylation (**Figs. 2(d) and 2(e)**).

This finding shows that histone modifications do more than recruit enzymes to specific genomic locations—they can directly activate those enzymes. The study also examined a DNMT3B mutation, R545C, found in advanced prostate cancer and showed that this mutant form is more readily activated, potentially leading to abnormal DNA methylation patterns.

By revealing how histone marks trigger DNMT3B activation, this research deepens our understanding of epigenetic communication within the cell. It also suggests new therapeutic possibilities: drugs that stabilize DNMT3B's inactive state could help prevent harmful DNA hypermethylation in disease, while molecules that mimic

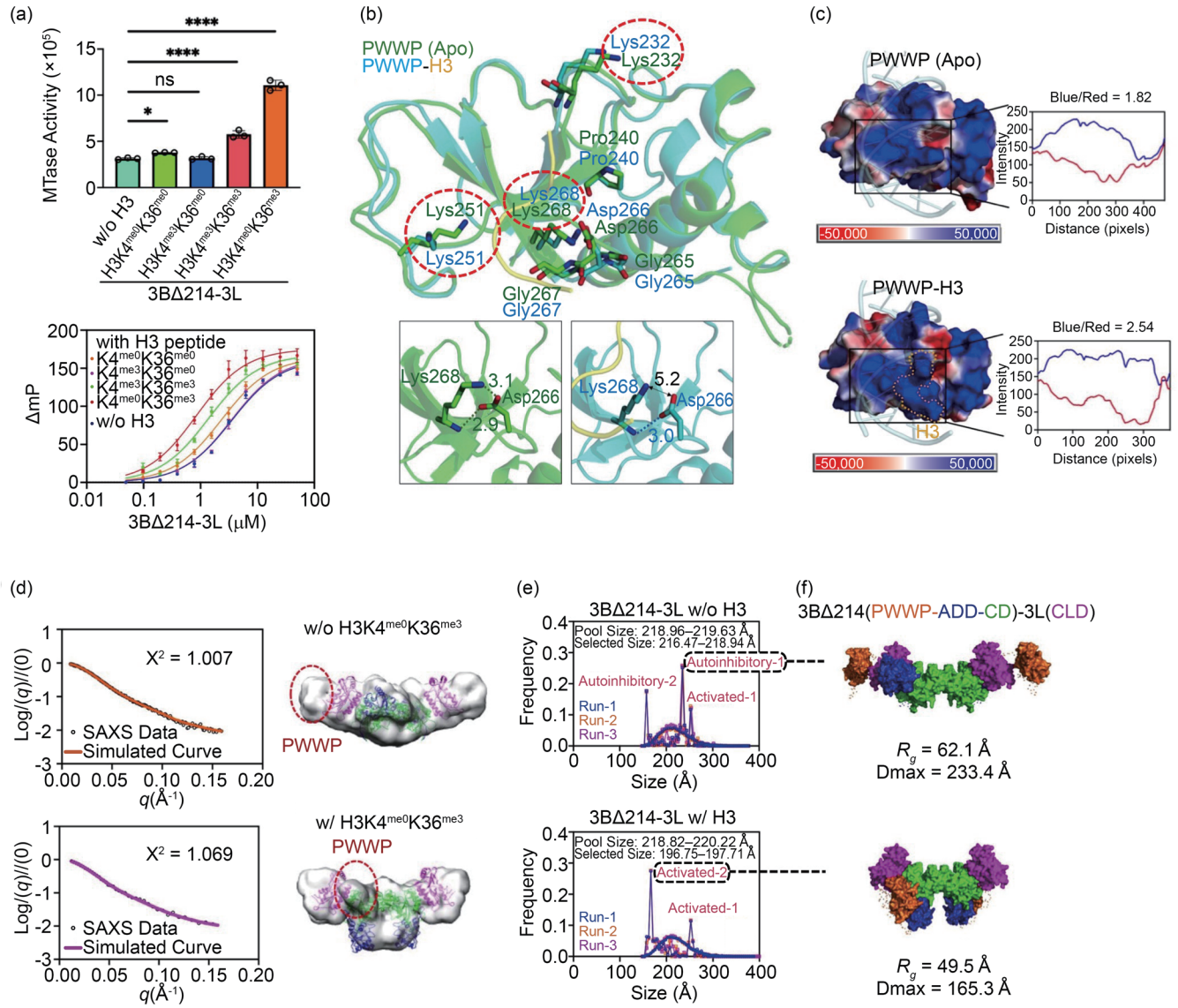

Fig. 2: Histone-driven structural remodeling activates DNMT3B. (a) Biochemical analyses demonstrate how histone H3 tail peptides with different methylation states at K4 and K36 affect the enzymatic and DNA-binding activities of DNMT3B. (b) Crystal structures of apo and H3-bound DNMT3B PWWP domains reveal differences in lysine side chain orientations (red dashed circles) and (c) corresponding surface potentials. (d) SAXS analyses of DNMT3B with and without the H3 peptide, with envelopes generated by GASBOR, indicate that DNMT3B undergoes conformational changes upon H3 binding. (e) Ensemble Optimization Method (EOM) analysis of SAXS data shows that DNMT3B adopts three predominant conformations in the absence of the H3 peptide and two predominant conformations in its presence. [Reproduced from Ref. 1]

activating histone signals might restore methylation where it is deficient. In summary, the study demonstrates that histone modifications not only guide DNMT3B to its DNA targets but also activate its enzymatic function. (Reported by Chao-Cheng Cho, Academia Sinica)

This report features the work of Hanna S. Yuan's team published in Sci. Adv. ***11****, eadu8116 (2025).*

TPS 05A Protein Microcrystallography
TPS 13A BioSAXS
TLS 15A1 Protein Crystallography

- X-ray Crystallography, SAXS
- Structural Biology, Protein Science

References

1. C. C. Cho, H. H. Huang, B. C. Jiang, W. Z. Yang, Y. N. Chen, H. S. Yuan, Sci. Adv. **11**, eadu8116 (2025).
2. C. C. Cho, C. Y. Fei, B. J. Jiang, W. Z. Yang, H. S. Yuan, Prot. Sci., **33**, e5131 (2024).
3. C. C. Cho, C. J. Lin, H. H. Huang, W. Z. Yang, H. Y. Lin, M. S. Lee, H. S. Yuan, ACS Chem. Biol. **18**, 1335 (2023).

Old Dogs and Their Ancient Tricks: How Cutting-Edge Structural Methods Gave Us New Insight into Ancient Molecules

Cutting-edge techniques revealed for the first time the undistorted atomic structure of ancient molecules when interacting with proteins in different redox states. These pristine structures permit a more detailed understanding of how proteins modulate energy conversion in biology.

From sensing their environments to metabolism, all living beings rely on proteins for their biological activities. However, for some special functions such as respiration, the electron transfer reaction by which animals transform food and oxygen into energy and waste products, proteins are insufficient. In these crucial cases, specialized molecules called cofactors are combined with proteins to expand the latter's functionality. Iron-sulfur clusters[1] (FeS, **Fig. 1(a)**) and flavins[2] (**Fig. 1(b)**) are two of the most ancient cofactors used during electron transfer. While FeS are small, inorganic compounds that accept or release a single electron (**Fig. 1(a)**), flavins, and more specifically flavin adenine dinucleotide (FAD), are larger organic molecules (**Fig. 1(b)**) with complex electron chemistry. In fact, FAD can either accept or donate up to two electrons, resulting in three possible redox states (**Fig. 1(b)**): fully depleted (FAD_{ox}), harboring one electron ($FAD^{\bullet-}$), or two ($FADH^-$).[3] Because of its redox versatility, proteins commonly use FAD as an adaptor between two-electron donors/acceptors, such as food-derived sugars and oxygen, and single-electron cofactors, such as FeS. Here, it has been suggested that proteins can modulate FAD and FeS redox properties *via* subtly changing their structures.

Given their enormous biochemical importance and intriguing structure-function relationship, FAD- and FeS-containing proteins have been extensively studied using structural methods such as X-ray crystallography and cryo-electron microscopy. However, both techniques release electrons during data collection, which are then captured by FAD and FeS cofactors.[4,5] Even a few milliseconds of data collection may alter the cofactor's redox state and cause structural distortions. This limitation in capturing native-like structures has left the natural mechanisms by which proteins interact with their cofactors under defined redox conditions unclear.

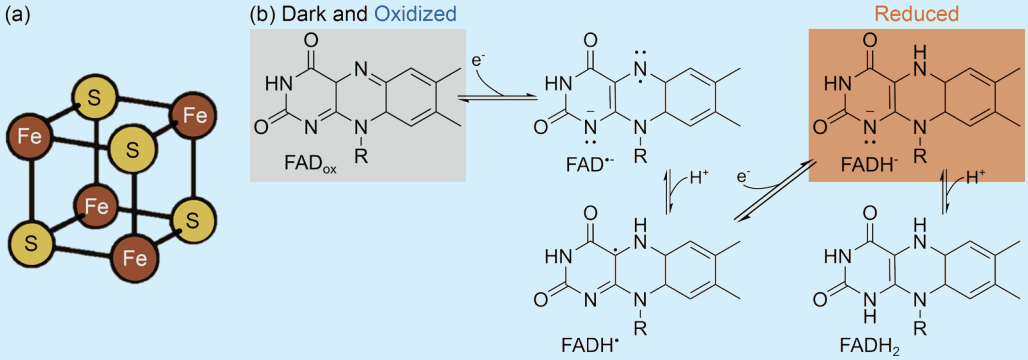

Fig. 1: The co-factors of *Cc*(6-4)PL. (a) The iron sulfur cluster FeS. An iron sulfur cluster consists of four sulfur and four iron atoms (yellow and orange, respectively), which arrange themselves in a cubic shape. The iron atoms then interact with the protein *via* sulfur-containing amino acids called cysteines. (b) The redox chemistry of FAD. Oxidized FAD (FAD_{ox}) transforms into $FAD^{\bullet-}$ by capturing an electron. $FAD^{\bullet-}$ can then evolve into $FADH^\bullet$ *via* addition of a proton (H^+). A second electron capture produces $FADH^-$ from $FADH^\bullet$. A final proton capture may produce $FADH_2$. In the dark-adapted and oxidized states, *Cc*(6-4)PL contains FAD_{ox} (grey shade), while in its reduced form, it contains $FADH^-$ (orange shade).

Here, an international research team led by Maestre-Reyna (National Taiwan University and Academia Sinica) and Essen (Philipps University Marburg, Germany) determined, for the first time, the structures of undistorted FeS and FAD working in tandem within a single protein, and in several different redox states (**Fig. 2**, see next page).[6] To do so, the international team used damage-free serial femtosecond crystallography (DF-SFX), a cutting-edge technique that can only be conducted in X-ray free electron lasers, special X-ray sources of which there are only five in the world. Because DF-SFX data collection is much faster than redox chemistry, the cofactors in structures obtained *via* DF-SFX maintain their native, redox-defined states.[7] For comparison purposes, the researchers also used the **TPS 05A** to produce radiation-damaged structures.

The chosen model system was the *Caulobacter crescentus* 64 photolyase (*Cc*(6-4)PL), an FAD-containing protein capable of using the energy of blue light to inject electrons into its flavin cofactor. Once the FAD is fully reduced ($FADH^-$), *Cc*(6-4)PL can then use the cofactor to repair mutated DNA. Interestingly, *Cc*(6-4)PL also contained a single FeS, whose function is not well understood.[8,9] To determine the *Cc*(6-4)PL undistorted structures of both the FAD and FeS in different redox states, and to determine whether the FeS redox chemistry depended on that of FAD, Prof. Maestre-Reyna's team collected the structure of *Cc*(6-4)PL in three different states. First, by performing the DF-SFX experiment in the dark, they collected dark-adapted *Cc*(6-4)PL (FAD_{ox}-FeS^{2+} state, **Fig. 2(a)**). By applying strong blue light and an electron donor, they induced full reduction of the FAD *via* illumination ($FADH^-$-FeS^{2+} state, **Fig. 2(a)**). Finally, by exposing the protein to an FeS-specific oxidizing agent, they obtained the oxidized *Cc*(6-4)PL structure (FAD_{ox}-FeS^{3+} state, **Fig. 2(a)**).

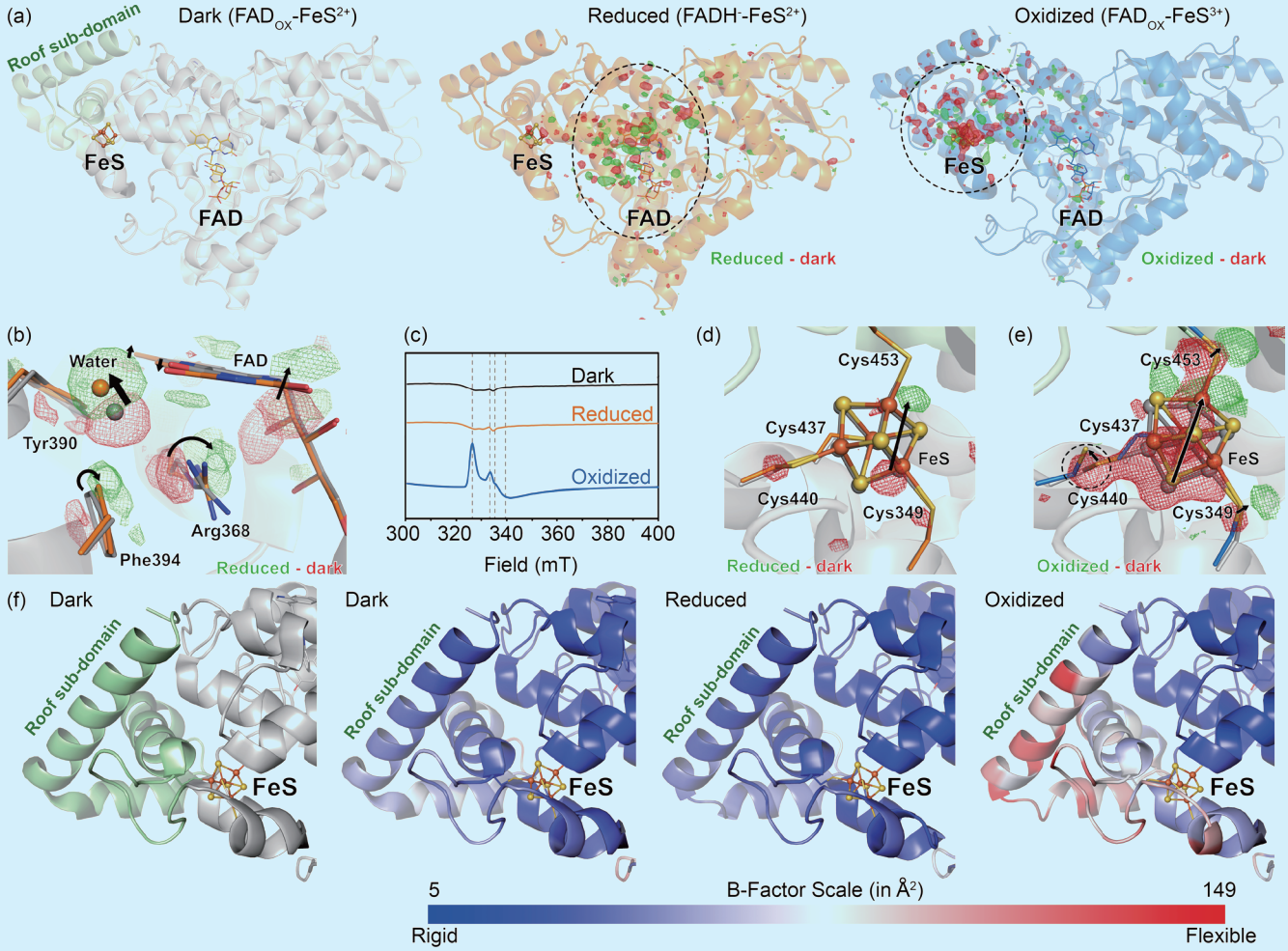

Fig. 2: The undistorted structures of *Cc*(6-4)PL in different redox states. (a) Global structures of *Cc*(6-4)PL in different redox states. Left: Dark-adapted state (grey cartoon with roof sub-domain shown in green), middle: reduced state (orange cartoon), right: oxidized state (blue cartoon). Difference electron density maps comparing the corresponding structure vs. the dark state are shown over the reduced and oxidized structures (green for positive peaks, red for negative ones). Difference electron density highlights where changes are occurring in the structure upon change of state, with negative features indicating locations from which atoms depart, while positive features where they move towards. The region of change is further highlighted with a black dashed circle. (b) Detail of the reduced vs. dark structural changes around the FAD binding site. Arrows indicate the direction of motion of individual amino acids (from negative towards positive density). Amino acids are shown as sticks (grey for dark, orange for reduced). (c) Electron paramagnetic resonance spectra of *Cc*(6-4)PL in the three redox states studied in this work (black for dark, orange for reduced, blue for oxidized). Notice that the dark and reduced states show the same spectrum, indicating no FeS redox change. The different shape of the spectrum in the oxidized state is indicative of oxidation of FeS. (d) Detail of the reduced vs. dark structural changes around the FeS binding site. Arrows indicate the direction of motion of individual amino acids (from negative towards positive density). Amino acids are shown as sticks, while FeS atoms as spheres (grey for dark, orange for reduced). (e) Detail of the oxidized vs. dark structural changes around the FeS binding site. Arrows indicate the direction of motion of individual amino acids (from negative towards positive density). Amino acids are shown as sticks, while FeS atoms as spheres (grey for dark, blue for oxidized). The broken protein–FeS bond is highlighted with a dashed black circle. (f) FeS redox state-dependent changes in the roof sub-domain. Left: Detail of the dark-adapted roof sub-domain shown as in (a). Right: Roof sub-domain in each of the *Cc*(6-4)PL, as indicated over each panel. Structures are shown as cartoons, and are colored by B-factor (blue to red), which is a measurement of protein flexibility. A color scale is provided below the panels. While the roof sub-domain is very rigid (blue) in the dark and reduced states, it is very flexible (red) in the oxidized state. [Adapted from Ref. 6]

By comparing the dark-adapted vs. reduced FAD states, the researchers found that the FAD underwent a "butterfly bend" along its three-membered ring moiety (**Fig. 2(b)**). Importantly, this redox state change induced dramatic changes in the *Cc*(6-4)PL protein, which compensated for the extra negative charge on $FADH^-$ by positioning a positively charged residue, Arginine R368, close to $FADH^-$ (**Fig. 2(b)**). Furthermore, a nearby water molecule moved away from the FAD upon reduction, suggesting that it acted as a proton donor during FAD reduction (**Figs. 2(b) and 1(b)**). Nearby aromatic residues also changed their conformation (**Fig. 2(b)**), supporting their role in electron transfer toward the FAD. Although independent electron paramagnetic resonance experiments (**Fig. 2(c)**) showed that FeS did not change its redox state in response to FAD transitioning to $FADH^-$, the team's research highlighted the tight correlation between FAD and FeS, as *Cc*(6-4)PL adaptation to $FADH^-$ resulted in subtle changes in FeS 3D structure (**Fig. 2(d)**). Conversely, *Cc*(6-4)PL responded to oxidation of FeS by partially breaking a single iron–protein bond (**Fig. 2(e)**). As a result, a *Cc*(6-4)PL region crucial for DNA recognition, the roof-like domain, became highly flexible (**Fig. 2(f)**), potentially impairing DNA binding. This revealed the structural basis by which FeS-containing DNA-binding proteins couple their ability to recognize DNA to the FeS redox state.

Overall, the joint research by the Maestre-Reyna and Essen groups revealed the structure–function relationship of a set of ancient cofactors by using the cutting-edge methodologies such as DF-SFX, showing for the first time how these old dogs perform their ancient tricks. Furthermore, their research has opened the path towards understanding the dynamics of FAD and FeS interlinked redox chemistry *via* time-resolved crystallographic methods. (Reported by Manuel Maestre-Reyna, National Taiwan University and Academia Sinica)

This report features the work of Manuel Maestre-Reyna and his collaborators published in J. Am. Chem. Soc. ***147****, 16084 (2025).*

TPS 05A Protein Microcrystallography

- Protein Crystallography
- Biological Macromolecules, Protein Structures, Life Science

References

1. R. Lill, Nature **460**, 831 (2009).
2. R. L. Fagan, B. A. Palfey. Elsevier Ltd, 37 (2010).
3. M. Maestre-Reyna, C. H. Yang, E. Nango, W. C. Huang, E. P. G. Ngurah Putu, W. J. Wu, P. H. Wang, S. Franz-Badur, M. Saft, H. J. Emmerich, H. Y. Wu, C. C. Lee, K. F. Huang, Y. K. Chang, J. H. Liao, J. H. Weng, W. Gad, C. W. Chang, A. H. Pang, M. Sugahara, S. Owada, Y. Hosokawa, Y. Joti, A. Yamashita, R. Tanaka, T. Tanaka, F. Luo, K. Tono, K. C. Hsu, S. Kiontke, I. Schapiro, R. Spadaccini, A. Royant, J. Yamamoto, S. Iwata, L. O. Essen, Y. Bessho, M. D. Tsai, Nat. Chem. **14**, 677 (2022).
4. E. F. Garman, Acta Crystallogr. D Biol. Crystallogr. **66**, 339 (2010).
5. V. Pfanzagl, J. H. Beale, H. Michlits, D. Schmidt, T. Gabler, C. Obinger, K. Djinović-Carugo, S. Hofbauer, J. Biol. Chem. **295**, 13488 (2020).
6. P. H. Wang, Y. Hosokawa, J. C Soares, H. J. Emmerich, V. Fuchs, N. Caramello, S. Engilberge, A. Bologna, C. J. Rosner, M. Nakamura, M. Watad, F. Luo, S. Owada, T. Tosha, J. Kang, K. Tono, Y. Bessho, E. Nango, A. J. Pierik, A. Royant, M. D. Tsai, J. Yamamoto, M. Maestre-Reyna, L. O. Essen, J. Am. Chem. Soc. **147**, 16084 (2025).
7. H. N. Chapman, C. Caleman, N. Timneanu, Phil. Trans. R. Soc. B **369**, 20130313 (2014).
8. K. Hitomi, K. Okamoto, H. Daiyasu, H. Miyashita, S. Iwai, H. Toh, M. Ishiura, T. Todo, Nucleic Acids Res. **28**, 2353 (2000).
9. I. Oberpichler, A. J. Pierik, J. Wesslowski, R. Pokorny, R. Rosen, M. Vugman, F. Zhang, O. Neubauer, E. Z. Ron, A. Batschauer, T. Lamparter, PLoS One **6**, e26775 (2011).

Near-Infrared-Activated Organic Nanocomposite for Enhanced Photothermal and Photodynamic Cancer Therapy

DTPT-core A–D–A nanoparticles (DTPTTCF@TPGS) exhibit low toxicity and potent near-infrared-triggered anticancer effects, effectively suppressing tumors.

Phototherapy, including photothermal therapy (PTT) and photodynamic therapy (PDT), has emerged as a minimally invasive and selective cancer treatment, leveraging localized heating or reactive oxygen species (ROS) generation to induce tumor cell death. PTT converts light energy into heat, causing DNA damage, protein denaturation, and membrane disruption, while PDT activates photosensitizers to produce ROS, triggering oxidative damage and apoptosis. Combining PTT and PDT enhances therapeutic efficacy, particularly when using near-infrared (NIR) light, which penetrates deeper into tissues. Organic acceptor–donor–acceptor (A–D–A) molecules with strong NIR absorption are promising phototherapeutic agents due to their high molar extinction coefficients, photostability, and dual PTT/PDT potential. However, their hydrophobic nature limits direct biomedical application, necessitating encapsulation in biocompatible carriers. D-α-tocopheryl polyethylene glycol succinate (TPGS) has proven effective, forming self-assembled nanoparticles (NPs) that improve solubility, stability, and bioavailability while also inhibiting P-glycoprotein to overcome drug resistance. TPGS-based NPs demonstrate low toxicity to normal cells, induce apoptosis in cancer cells *via* ROS generation, and enhance the therapeutic effects of co-delivered anticancer agents. These features make TPGS-encapsulated A–D–A molecules a versatile and promising platform for multimodal NIR-triggered phototherapy, combining high efficacy, selectivity, and safety for potential clinical applications.

Jiashing Yu and Ken-Tsung Wong (National Taiwan University) recently initiated a collaborative study to investigate a series of A–D–A structured small molecules featuring a coplanar dithieno[2,3-d:2′,3′-d′]thieno[3,2-b:3′,2′-b′]dipyrrole (DTPT) core, a framework known for its excellent charge-transport properties and strong NIR light absorption. Although DTPT-based materials have been extensively explored for applications in organic photovoltaics and other optoelectronic devices, this study repurposes them as organic photosensitizers for cancer phototherapy. To improve biocompatibility and stability, the DTPT-based molecules were formulated into NPs using TPGS (**Fig. 1(a)**). Among the series, DTPTTCF—bearing 3-cyano-4,5,5-trimethylfuran-2(5H)-ylidene malononitrile (TCF) terminal acceptor groups—exhibited the most promising performance.

Photothermal characterization revealed that, upon 808 nm laser irradiation for 10 minutes, most DTPT-based nanoparticles (excluding DTPTCY@TPGS) exhibited a temperature increase exceeding 20 °C at a concentration of 30 ppm, whereas the control (water) showed no measurable change. Comparable heating behavior was observed in phosphate-buffered saline (PBS) (**Fig. 1(b)**), confirming the strong photothermal capabilities of these nanoparticles. To assess cytotoxicity, an *in vitro* assay was conducted on both normal (L929) and cancerous (4T1) cell lines. The results demonstrated that L929 cell viability remained above 65% even at a high concentration of 50 ppm, indicating minimal toxicity toward normal cells. Similarly, 4T1 cells treated with DTPTTCF NPs maintained over 50% viability at the same concentration, suggesting limited cytotoxic

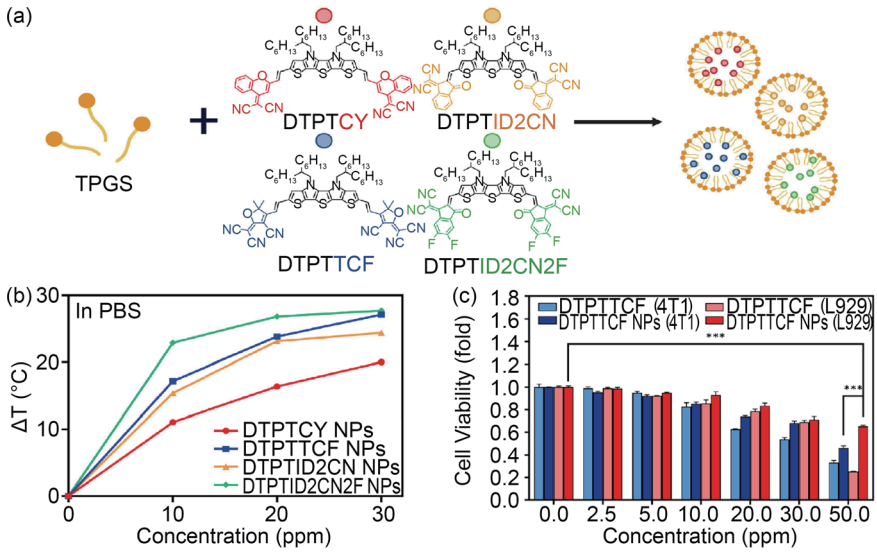

Fig. 1: (a) Schematic of tailor-made nanoparticles as photosensitizers. (b) Temperature increase of DTPT NPs in PBS after 10 minutes of irradiation with an 808 nm laser. (c) Cell viability of 4T1 and L929 cells incubated with DTPTTCF@TPGS NPs at different concentrations (mean ± SD, n = 3, $p < 0.001$ by ANOVA followed by Tukey's post hoc test). [Reproduced from Ref. 1]

effects on cancer cells. Collectively, these findings underscored the biocompatibility of DTPTTCF NPs and their low cytotoxicity toward both normal and malignant cells (**Fig. 1(c)**).

Overall, the resulting DTPTTCF@TPGS nanoparticles exhibited low inherent cytotoxicity, strong NIR absorption, enhanced photothermal conversion efficiency, and robust photodynamic activity, making them promising candidates for cancer phototherapy.

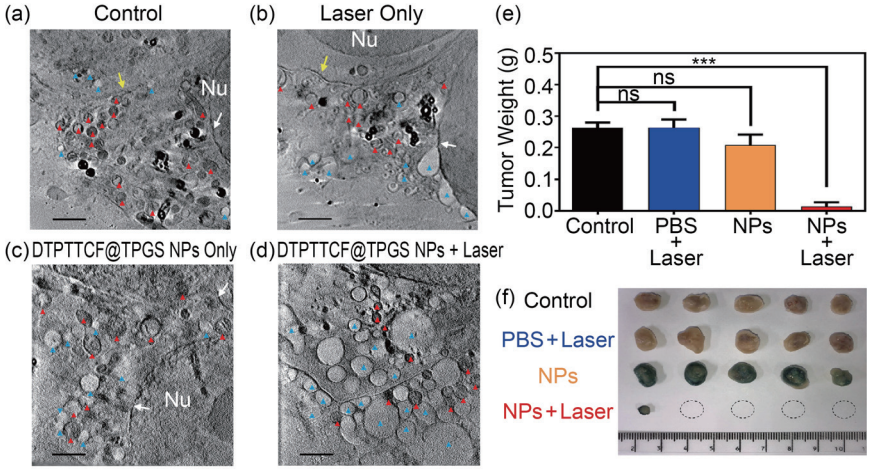

Fig. 2: Virtual slices of reconstructed Z-stack images of 4T1 cells under different treatment conditions captured *via* soft SXT: (a) control group, (b) laser-only group, (c) DTPTTCF@TPGS NPs-only group, and (d) NPs + Laser group. Nu: nucleus; mitochondria (red); vesicles (blue); nuclear membrane (white arrows); cell membrane (yellow arrows). Scale bars: 2 μm. (e) Tumor weight of mice at the end of treatments (day 14) (mean ± SD, n = 5, $p < 0.001$ by ANOVA followed by Tukey's post hoc test). (f) Photographs of tumors extracted from mice at the end of treatments (n = 5). [Reproduced from Ref. 1]

Additionally, soft X-ray tomography (SXT) at **TPS 24A** beamline was employed to visualize treatment-induced intracellular alterations with high spatial resolution (**Figs. 2(a)–2(d)**). In 4T1 cells, major organelles—including mitochondria, vesicles, nuclei, nuclear envelopes, and plasma membranes—were clearly delineated, enabling the precise assessment of morphological integrity. No appreciable structural differences were detected between the control and laser-only groups, indicating that laser irradiation alone did not perturb cellular ultrastructure. By contrast, subtle vacuolar changes were observed in a small subset of cells within the NPs-only group, suggesting limited nanoparticle-associated stress. Notably, extensive and prominent vacuolization emerged following irradiation in the NPs + Laser group, representing a marked deviation from all other conditions. Taken together, these SXT observations strongly support that the combined NPs + Laser treatment triggered pronounced intracellular disruption consistent with the initiation of apoptotic cell death.

In vivo antitumor performance was evaluated using a 4T1 tumor model established in BALB/c mice. Treatment began when tumors reached 30–60 mm^3, and mice were assigned to four groups: PBS (control), PBS with NIR laser, DTPTTCF@TPGS NPs, or NPs combined with NIR laser irradiation. Only the NPs + Laser group showed a pronounced therapeutic effect. After intratumoral injection, NIR irradiation of NPs-treated tumors rapidly increased tumor temperature to approximately 55 °C, enabling effective photothermal activity. Throughout the 14-day observation period, tumor progression differed significantly among groups: tumors in the control, PBS + Laser, and NP-only groups expanded at least four-fold from baseline. By contrast, the NPs + Laser group exhibited strong inhibition of tumor growth, with only one very small tumor remaining out of five mice (**Fig. 2(e)**). At the end of treatment, excised tumors showed dramatic reductions in tumor weight, with nearly complete tumor elimination in the NPs + Laser group (**Fig. 2(f)**). Overall, laser-activated DTPTTCF@TPGS NPs markedly reduced both tumor size and tumor weight, demonstrating excellent photothermal antitumor efficacy.

In summary, a long-wavelength-responsive phototherapeutic delivery system was developed based on DTPT-centered A–D–A-type conjugated molecules. These molecules exhibited strong absorption, efficient reactive oxygen species generation, and pronounced photothermal effects. Utilizing the self-assembly properties of amphiphilic TPGS, biocompatible DTPTTCF@TPGS nanoparticles with high loading efficiency were formulated. *In vitro* assays demonstrated controlled and effective cytotoxicity against cancer cells, while high-resolution imaging revealed significant intracellular damage under NIR irradiation. Overall, these results underscored the potential of DTPTTCF@TPGS nanoparticles as robust and precise phototherapeutic agents for cancer treatment. (Reported by Zi-Jing Lin)

This report features the work of Jiashing Yu, Ken-Tsung Wong and their collaborators published in Adv. Healthcare Mater. ***14****, 2404418 (2025).*

TPS 24A Soft X-ray Tomography

- Soft X-ray Imaging, SXT
- Biomedical/Biological Science, Biomedical Engineering, Materials Science, Environmental Science

Reference

1. M.-H. Liu, Z.-J. Gao, W.-Y. Huang, C.-H. Hsiao, V. Chen, L.-J. Lai, Z.-J. Lin, M. D.-S. Hua, C.-C. Hsieh, E.-Y. Chuang, J.-S. Yu, K.-T. Wong. Adv. Healthcare Mater. **14**, 2404418 (2025).

ScdA: Unveiling the Nitrite-Reducing Machinery That Helps *Staphylococcus aureus* Survive

A tri-disciplinary team uncovered how the elusive ScdA protein in Staphylococcus aureus forms a dimeric structure to generate nitric oxide, revealing a new mechanism of bacterial stress resistance.

For nearly two decades, the enigmatic di-iron protein ScdA of *Staphylococcus aureus (S. aureus)* puzzled microbiologists. Identified in 2008 and grouped within the "repair of iron centers" family, ScdA was believed to protect the bacterium's iron-sulfur enzymes from oxidative and nitrosative damage.[1] Yet, despite its presumed importance in the pathogen's defense against immune attack, no one had ever visualized the protein's complete structure, or fully understood what it actually did.

A recent study published in the *Journal of the American Chemical Society* (2025) answers both questions.[2] The researchers revealed that ScdA is not merely a repair enzyme, but it is a nitrite reductase that transforms nitrite (NO_2^-) into nitric oxide (NO), a reactive molecule with profound biological consequences. By combining X-ray crystallography, solution-state nuclear magnetic resonance (NMR), AlphaFold modeling, and pulsed electron spin resonance (ESR)/double electron–electron resonance (DEER) spectroscopy, they reconstructed the first full-length structure of dimeric ScdA and linked its architecture directly to its catalytic function.

A Long-Standing Mystery in Bacterial Stress Biology

S. aureus—a major human pathogen and the source of methicillin-resistant infections (MRSA)—endures some of the harshest chemical assaults mounted by the immune system. Host macrophages generate reactive oxygen and nitrogen species to damage bacterial macromolecules. ScdA is expressed as a stress response, regulated by the two-component system SrrAB. Although earlier studies hinted that ScdA repaired damaged iron-sulfur clusters, the details of its structure and mechanism of action remained elusive.

The central question persisted: Was ScdA merely a repair enzyme, or did it play a more active role in managing nitrosative stress?

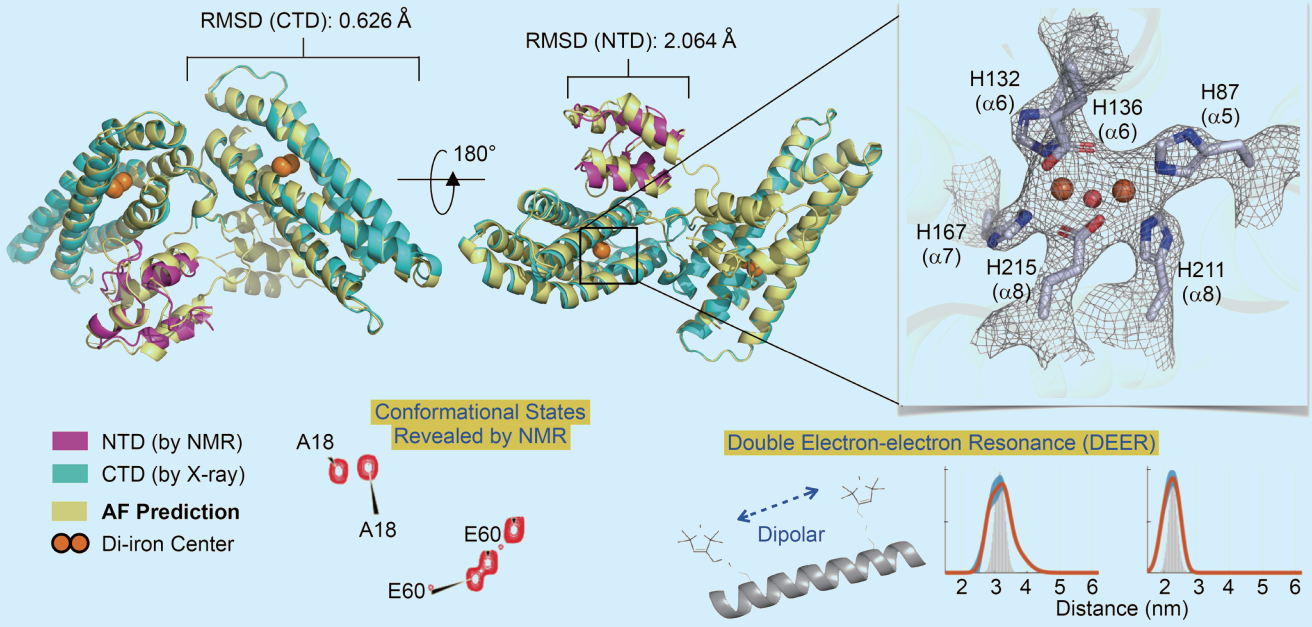

Fig. 1: Integrative structural model of full-length ScdA constructed from X-ray crystallography, NMR spectroscopy, and DEER distance measurements. The CTD di-iron domain (cyan) was resolved by X-ray diffraction at the NSRRC, the NTD domain (magenta) by NMR, and the composite model (yellow) refined with AlphaFold and DEER constraints. The di-iron catalytic center (orange spheres) and coordinating residues are shown in electron density maps. RMSD values indicate high structural convergence for the CTD (0.626 Å) and moderate flexibility in the NTD (2.064 Å). DEER-derived distance distributions and spin-labeling schematics demonstrate how pulsed ESR measurements define domain orientations and validate the dimeric architecture of ScdA. [Reproduced from Ref. 2]

To answer this, the researchers needed not only high-resolution structural data but also insight into how the protein behaves in solution and during catalysis. Solving the full-length structure of ScdA required three complementary approaches and an exceptional collaboration across institutions.

Seeing the Whole Picture: A Three-Way Collaboration

The C-terminal domain (CTD) of ScdA, which contains the di-iron catalytic center, was the first piece to fall into place. After more than three years of work, the team obtained crystals suitable for X-ray diffraction and collected crystallographic data at **TPS 05A** in the NSRRC. The resulting structure revealed a compact four-helix bundle containing six conserved residues—histidines and glutamates—that coordinate the two iron atoms (**Fig. 1**).

The N-terminal domain (NTD), by contrast, refused to crystallize. Using high-field NMR spectroscopy, they determined that this flexible region adopts a smaller helical fold. To bridge these two structural fragments, the team employed AlphaFold-3 predictions to generate a full-length model and validated it experimentally using DEER spectroscopy (**Fig. 1**).

DEER, an advanced pulsed ESR technique, measures nanometer-scale distances between spin labels placed on the protein surface.[3,4] Using site-directed spin labeling of ScdA, they mapped inter-residue distances across both domains, confirming that ScdA exists as a homodimer in solution. The DEER-derived distance distributions closely matched those predicted by AlphaFold, establishing the model as a realistic representation of ScdA's dynamic structure.

This integrative approach—X-ray, NMR, and DEER—was possible only through the collaboration of three research groups: Yun-Wei Chiang (ESR/DEER, National Tsing Hua University), Shih-Che Sue (NMR, National Tsing Hua University), and Nien-Jen Hu (X-ray crystallography, National Chung Hsing University). Each method resolved a different aspect of ScdA's architecture; together they revealed the complete molecular geometry (**Fig. 1**).

From Structure to Function: ScdA Generates Nitric Oxide

With the structure in hand, the researchers turned to investigate function. Spectroscopic and kinetic experiments showed that ScdA catalyzes the reduction of nitrite to nitric oxide at its di-iron center. Ultraviolet–visible spectra revealed the formation of an iron–nitrosyl complex upon nitrite addition, while low-temperature EPR spectra displayed distinct signatures of mononitrosyl and dinitrosyl intermediates.

Kinetic experiments indicated robust nitrite-to-NO turnover comparable to other bacterial nitrite reductases. Interestingly, ScdA's dimeric form exhibited higher catalytic efficiency than its monomeric variants, suggesting that dimerization tunes electron transfer and substrate binding. Mutating a key interface residue (Ser77) disrupted dimer formation and reduced enzymatic performance, underscoring the functional importance of the dimeric assembly (**Fig. 2**, see next page).

Nitric Oxide: A Double-Edged Sword

Nitric oxide is a paradoxical molecule—both a weapon and a hazard. In the immune system, it serves as an antimicrobial agent, yet at controlled levels, it also acts as a signaling molecule. In-cell assays revealed that *Escherichia coli* engineered to overexpress ScdA suffered severe growth inhibition in nitrite-rich environments, demonstrating the cytotoxic potential of ScdA-generated NO.

In *S. aureus*, however, ScdA's activity is likely tightly regulated, enabling the bacterium to harness small, localized bursts of NO to modulate its redox balance without succumbing to toxicity. Understanding how this regulation operates could open new routes to antimicrobial intervention by destabilizing this balance, researchers may be able to sensitize MRSA and related pathogens to immune defenses.

A Technological and Biological Milestone

Beyond its biological insights, the study showcases the power of integrative structural biology. Advanced pulsed ESR/DEER spectroscopy provided the crucial link that unified data from X-ray and NMR studies, demonstrating how modern ESR can visualize entire protein architectures that are otherwise inaccessible. The approach offers a general blueprint for mapping large, multi-domain complexes whose flexibility frustrates traditional crystallography.

From a societal standpoint, the implications reach far beyond one bacterial enzyme. Understanding how pathogens like *S. aureus* regulate reactive nitrogen chemistry could inform strategies for next-generation antibiotics or redox-modulating

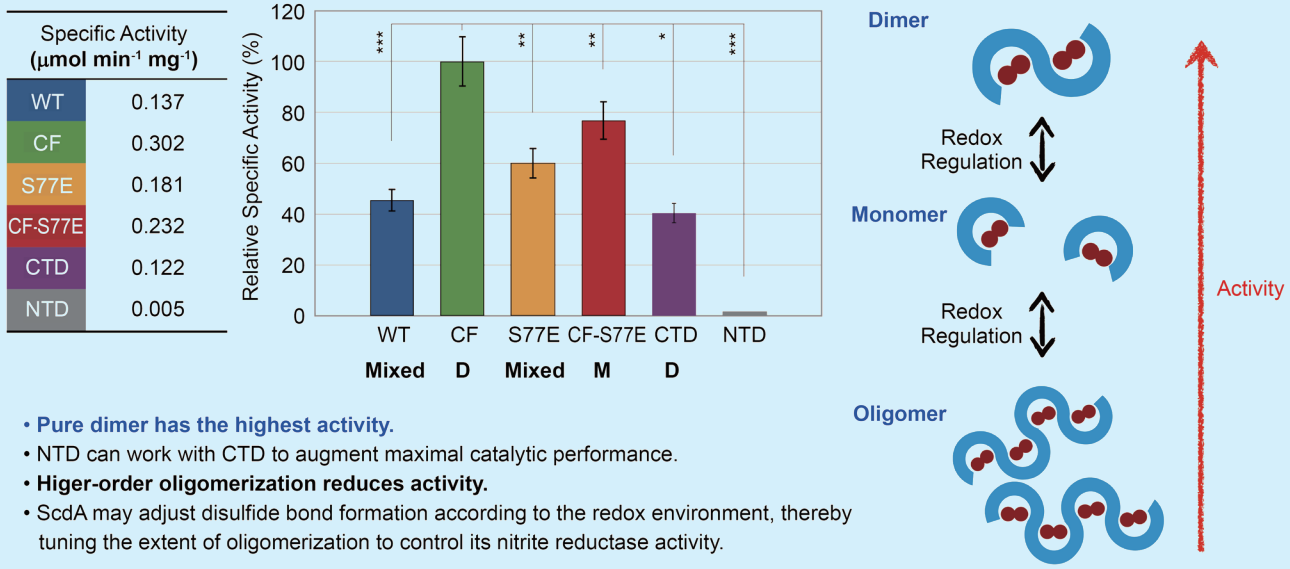

Fig. 2: Redox-dependent oligomerization governs the catalytic efficiency of ScdA. The bar chart compares nitrite reductase activities of wild-type and mutant variants. The cysteine-free (CF) ScdA, which forms a stable dimer, exhibits the highest activity by avoiding disulfide-linked oligomerization that otherwise suppresses catalysis. The S77E mutation, located at the dimer interface, disrupts dimer formation and stabilizes the disulfide-linked oligomeric state, resulting in reduced activity. CF-S77E stabilizes the monomeric state. Schematics on the right illustrate how redox regulation modulates transitions among oligomeric, dimeric, and monomeric forms, thereby fine-tuning enzymatic output. These findings indicate that ScdA adjusts its disulfide bonding and oligomerization state in response to redox conditions to optimize nitrite reductase activity. [Reproduced from Ref. 2]

therapies. ScdA—once an obscure stress-response protein—now emerges as a key player in bacterial survival and a potential target for antimicrobial design. (Reported by Nien-Jen Hu, National Chung Hsing University; Shih-Che Sue and Yun-Wei Chiang, National Tsing Hua University)

This report features the work of Yun-Wei Chiang and his collaborators published in J. Am. Chem. Soc. ***147****, 31558 (2025).*

TPS 05A Protein Microcrystallography

- Protein Crystallography
- Biological Macromolecules, Protein Structures, Life Science

References

1. T. W. Overton, M. C. Justino, Y. Li, J. M. Baptista, A. M. P. Melo, J. A. Cole, L. M. Saraiva, J. Bacteriol. **190**, 2004 (2008).
2. H.-Y. Chen, R.-F. Tsai, Y.-S. Lu, Y.-C. Cheng, H.-Y. Fan-Chiang, C.-Y. Wu, F.-C. Lo, H.-W. Kuo, W.-K. Yang, W.-Y. Liao, N.-J. Hu, S.-C. Sue, Y.-W Chiang, J. Am. Chem. Soc. **147**, 31558 (2025).
3. P.-S. Yeh, C.-C. Li, Y.-S. Lu, Y.-W. Chiang, JACS Au **3**, 2918 (2023).
4. C.-C. Cheng, R.-F. Tsai, C.-K. Lin; K.-T. Tan, V. Kalendra, M. Simenas, C.-W. Lin, Y.-W Chiang, JACS Au **4**, 3766 (2024).

Breaking the Mold: A Distinct Class of Terpenoid Cyclases Redefines Abscisic Acid Biosynthesis

The crystal structures of BcABA3 and its homologs reveal a distinct class of terpenoid cyclases that lack canonical motifs. This enzyme architecture is characterized by a unique glutamate-chelated Mg^{2+} cluster and a distal Zn^{2+} anchor, which enable fungal abscisic acid biosynthesis and provide a versatile platform for the production of novel bacterial terpenoids.

Terpenoid cyclases (TCs) are the molecular architects behind the most diverse family of natural products, orchestrating the complex cyclization of linear isoprenoid precursors into intricate ring structures. For decades, the biochemical understanding of this enzyme family has been grounded in a strict structural requirement: the presence of aspartate-rich motifs, such as DDXXD or NSE/DTE.[1] These motifs are considered indispensable for coordinating the divalent metal ions (typically Mg^{2+}) that trigger the ionization of the substrate's pyrophosphate group. However, nature often defies established rules. The discovery of BcABA3, a key enzyme in the phytopathogenic fungus *Botrytis cinerea*, challenged this paradigm. Unlike plants, which synthesize the stress hormone abscisic acid (ABA) indirectly from carotenoids, these fungi utilize a direct pathway involving the cyclization of farnesyl pyrophosphate (FPP) by BcABA3.[2] Despite catalyzing a classic sesquiterpene cyclization, BcABA3 lacks the signature aspartate-rich motifs.[3] To elucidate the molecular basis of this evolutionary anomaly, the research team led by Rey-Ting Guo (Hangzhou Normal University, China) solved the high-resolution crystal structures of BcABA3 and its homologs using diffraction data collected at **TPS 05A** and **TPS 07A** of the NSRRC.

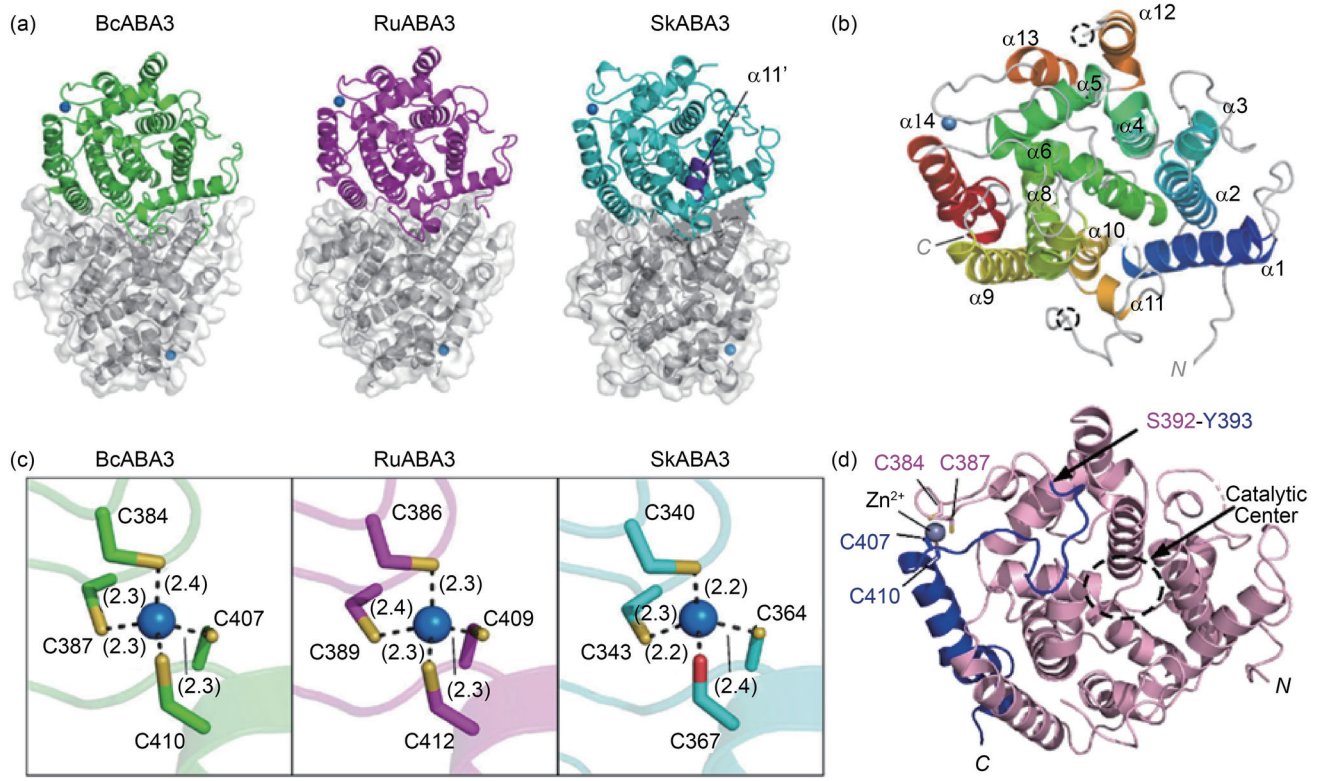

Fig. 1: Structural architecture and essential distal zinc anchor of ABA3-like TCs. (a) Comparative overall structures of the fungal BcABA3 and RuABA3 and the bacterial SkABA3. Despite their diverse origins, all three display a highly conserved homodimeric configuration. (b) Topology of a single BcABA3 polypeptide chain. The enzyme exhibits an all-α-helix fold (labeled α1–α14), featuring a unique C-terminal extension (α11–α14), which is characteristic of this cyclase class. (c) Close-up view of the metal coordination site on the loop between helices α13 and α14. The zinc ion (Zn^{2+}, blue sphere) is coordinated in a tetrahedral geometry by conserved cysteine residues, forming a structural motif distant from the active center. (d) Structural role of the Zn^{2+} site. The loop containing the Zn-binding motif extends to cover the top of the catalytic center (indicated by the dashed circle). The blue region corresponds to the C-terminal segment absent in BcABA3-S, a naturally occurring short variant. The inactivity of this truncated variant demonstrates that the Zn-stabilized cap is essential for maintaining active site integrity. [Reproduced from Ref. 4]

The path to determining these structures required overcoming significant challenges in protein stability. Initial attempts to crystallize full-length BcABA3 were hampered by the protein's labile nature. By employing a strategy of N-terminal truncation and utilizing the more stable homolog RuABA3 (from *Rutstroemia sp.*), the team successfully determined the structures of BcABA3, RuABA3, and a bacterial homolog, SkABA3 (from *Shimazuella kribbensis*) (**Fig. 1(a)**). Structural analysis reveals that this distinct class of TCs adopts an all-α-helix fold. While the N-terminal topology (helices α1–α10) resembles that of canonical TCs, the C-terminal region is uniquely extended with four additional helices (α11–α14) (**Fig. 1(b)**). A striking feature was identified within the extensive loop connecting helices α13 and α14: a specific metal-binding site coordinated in a tetrahedral geometry by cysteine residues (**Fig. 1(c)**). Atomic spectrometric analysis confirmed this to be a Zinc (Zn^{2+}) ion. Although located remotely from the active center, mutagenesis data indicate that this Zn^{2+} site functions as a crucial structural anchor. It stabilizes the loop extending over the active site, maintaining the architectural integrity required for catalysis, a finding consistent with the inactivity of natural variants lacking this C-terminal region (**Fig. 1(d)**).[3]

The most significant departure from canonical enzyme mechanisms is found in the architecture of the active site. By determining the complex structures of RuABA3 with a substrate analog (FSPP) and SkABA3 with the reaction product (PPi) (**Fig. 2(a)**), the researchers identified a novel metal-binding strategy. In the complete absence of aspartate-rich motifs, these enzymes utilize a strictly conserved glutamate residue (E124 in BcABA3) to coordinate the Mg^{2+} cluster required for substrate ionization (**Fig. 2(b)**). Additionally, the molecular recognition of the pyrophosphate moiety is mediated by a distinctive arrangement of residues: four basic residues (R202, K249, H250, and R312) and two tyrosine residues (Y242 and Y313) establish a precise hydrogen-bond network (**Fig. 2(b)**). This network features a conserved arginine-tyrosine (RY) pair. While RY pairs are common in Type I TCs, the pair in BcABA3 serves a dual function by interacting

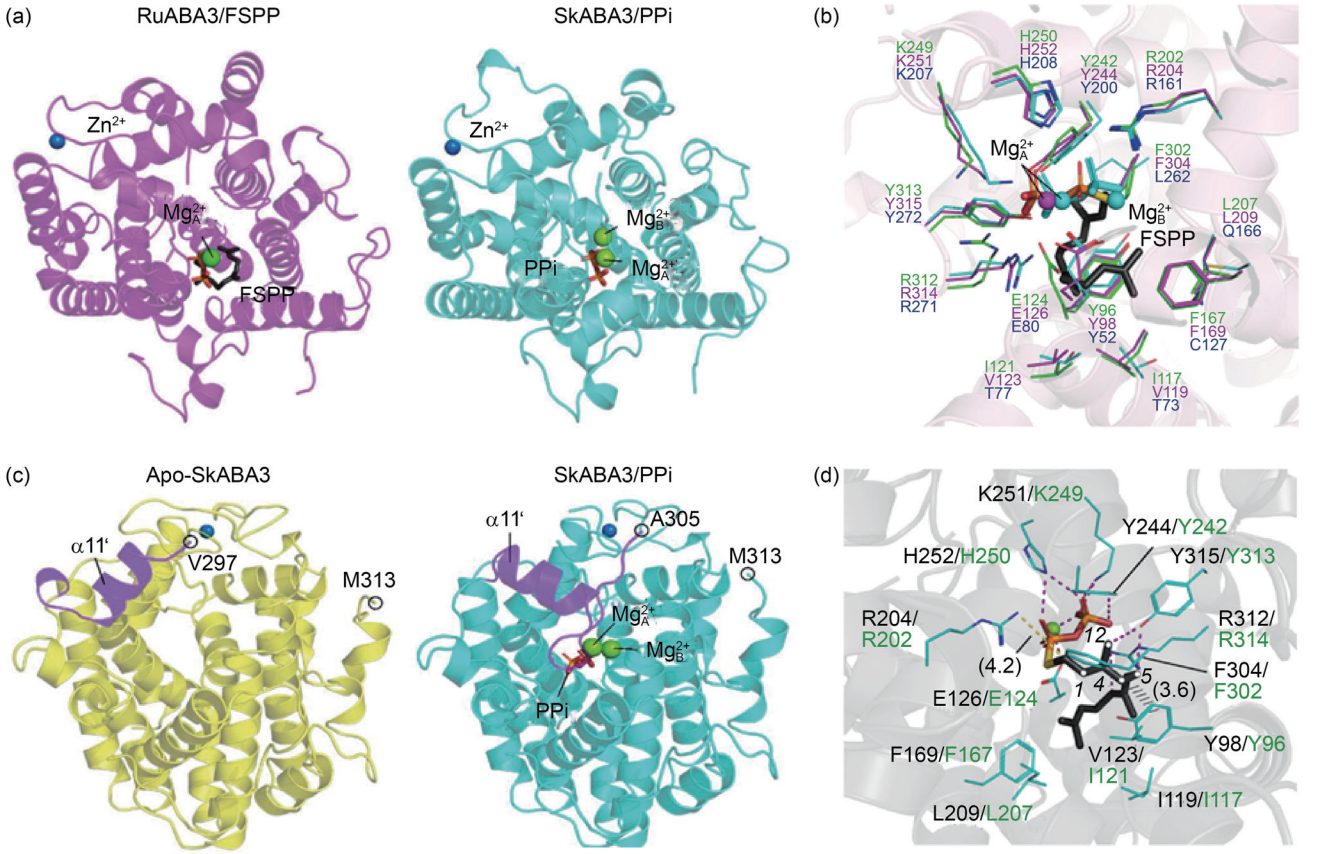

Fig. 2: Unique active site architecture and catalytic mechanism of ABA3-like cyclases. (a) Structures of RuABA3 bound to the substrate analog FSPP (magenta) and SkABA3 bound to the product PPi (cyan) show the ligand positioned deep within a central hydrophobic pocket. (b) Comparison of the substrate-binding pockets of apo-BcABA3 (green), RuABA3-FSPP (magenta), and SkABA3-PPi (cyan) demonstrates that, in the absence of a canonical aspartate-rich motif, a strictly conserved glutamate residue coordinates the Mg^{2+} cluster (spheres) required for catalysis. The pyrophosphate group is stabilized by a unique arrangement of basic residues and tyrosines, differing from classical TCs. (c) Substrate-driven conformational changes in SkABA3: upon ligand binding, helix α11' rotates approximately 90° (purple), positioning the adjacent loop region to cover the active site, which likely protects reactive carbocation intermediates. (d) The proposed substrate interaction network in the RuABA3-FSPP complex: the aromatic ring of residue Y96 (and Y98 in SkABA3) provides critical packing interactions that stabilize the hydrocarbon tail of the substrate. Mutagenesis studies indicate that this specific shaping of the hydrophobic pocket is essential for directing the cyclization cascade. [Reproduced from Ref. 4]

with both the pyrophosphate group and the hydrocarbon portion of the substrate.

A detailed structural comparison further revealed the dynamic features of the catalytic cycle. In the SkABA3 structure, helix α11' rotates by approximately 90° upon ligand binding, accompanied by the movement of a loop that closes over the active site (**Fig. 2(c)**). This induced-fit mechanism likely protects the highly reactive carbocation intermediates from premature quenching by the solvent. The reaction proceeds through a distinct pathway involving neutral intermediates, such as (E)-β-farnesene and allofarnesene.[3] The study demonstrated that the shape of the hydrophobic pocket directs this cascade; residues such as Y96 provide critical packing interactions to stabilize intermediates (**Fig. 2(d)**). Mutation of these pocket-lining residues altered the reaction pathway, causing the enzyme to stall and release intermediates rather than the final product.

The characterization of the bacterial homolog SkABA3 further broadens the biological significance of this work. Although SkABA3 shares the same "ABA3-like" fold and active site features, it produces a chemically distinct and uncharacterized sesquiterpenoid isomer. This demonstrates that the newly defined enzyme class is not confined to fungal ABA biosynthesis but instead represents a versatile evolutionary platform for synthesizing diverse natural products. Since terpenoids are a major source of pharmacological agents—including essential antibiotics and chemotherapeutics—this finding has considerable potential for pharmaceutical applications. Using the structural blueprint of ABA3, researchers can now search microbial genomes for similar cryptic enzymes, potentially leading to the discovery of new therapeutic lead compounds. These structural insights collectively establish a foundation for discovering and engineering novel bioactive compounds within the extensive microbial terpenoid repertoire. (Reported by Chun-Hsiang Huang, NSRRC)

This report features the work of Rey-Ting Guo and his collaborators published in Nat. Commun. ***16****, 207 (2025).*

TPS 05A Protein Microcrystallography
TPS 07A Micro-focus Protein Crystallography

- Protein Crystallography
- Biological Macromolecules, Protein Structures, Life Science

References

1. D. W. Christianson, Chem. Rev. **117**, 11570 (2017).
2. V. Siewers, L. Kokkelink, J. Smedsgaard, P. Tudzynski, Appl. Environ. Microbiol. **72**, 4619 (2006).
3. J. Takino, T. Kozaki, Y. Sato, C. Liu, T. Ozaki, A. Minami, H. Oikawa, J. Am. Chem. Soc. **140**, 12392 (2018).
4. S. Li, J.-W. Huang, J. Min, H. Li, M. Ning, S. Zhou, Y. Yang, C.-C. Chen, R.-T. Guo, Nat. Commun. **16**, 207 (2025).

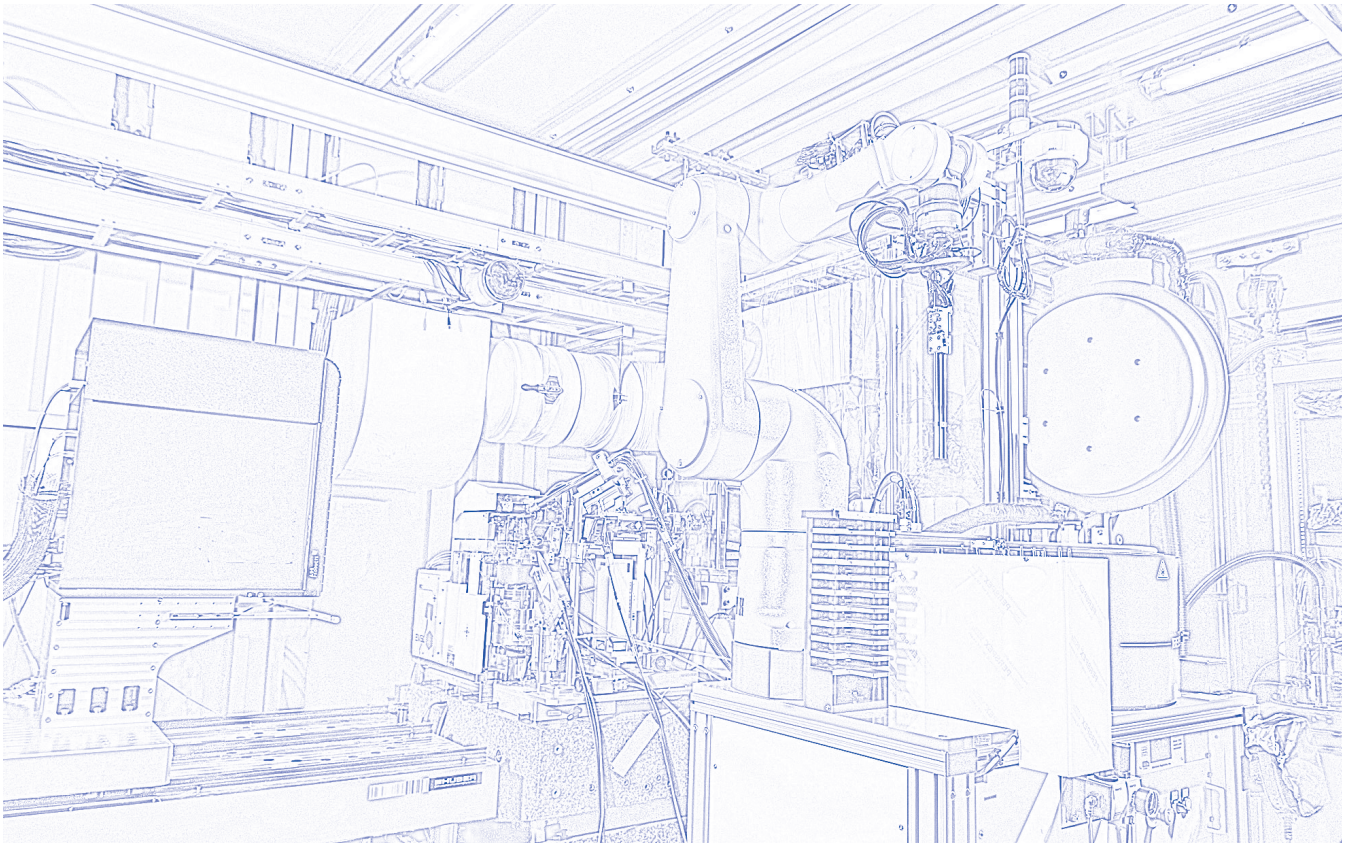

Infrared Clues That Help Track Lupus Nephritis Over Time

A label-free infrared method enables clinicians to quickly and precisely track kidney inflammation.

Monitoring lupus nephritis (LN) has long been one of the most difficult challenges in autoimmune medicine. Standard laboratory biomarkers often change too slowly to reflect real-time kidney inflammation, while a kidney biopsy is invasive and unsuitable for frequent monitoring. In response to this gap, a collaborative team led by Mei-Ching Yu (Lin-Kou Chang Gung Memorial Hospital) and Yao-Chang Lee (NSRRC) has developed an innovative infrared (IR) spectroscopic approach that reveals LN activity from a simple drop of serum, without the need for labels or chemical reagents. Their study introduces a practical and patient-friendly tool with the potential to transform how clinicians evaluate disease progression and therapeutic response.[1]

The new method relies on attenuated total reflection Fourier-transform infrared (ATR-FTIR) spectroscopy, performed at the **TLS 14A1** IR beamline. Rather than using only static spectral snapshots, the team monitored how serum IR absorption bands change during a controlled dehydration process. These time-resolved signals contain subtle biochemical information—such as IgG glycosylation, lactate levels, protein hydrophobicity, and albumin content—that closely correlate with LN disease activity. To quantify these changes, the researchers introduced a metric called the Relative Absorption Difference (RAD) and defined a measurable RAD gap, representing the difference between early-stage and late-stage values of each spectral marker during dehydration. **Figure 1** shows how the method captures biochemical fingerprints spanning carbohydrates, amino acids, lipids, and protein backbones. These spectral markers include (1) a glycosylation-related band at 1030 cm^{-1}, (2) a lactate band at 1121 cm^{-1}, (3) protein hydrophobic/hydrophilic signatures near 2930–2960 cm^{-1} and 1546–1650 cm^{-1}, and (4) albumin-related vibrations around 1400–1450 cm^{-1}. When analyzed together, these markers provide a comprehensive, label-free biochemical profile of patient serum.

$$\mathbf{RAD}(\nu_1, \nu_2, t, T) = \frac{\mathbf{PH}_1(\nu_1, t, T) - \mathbf{PH}_2(\nu_2, t, T)}{\mathbf{PH}_1(\nu_1, t, T)}$$

Hydrophobicity (Hp) $\frac{\mathbf{PH}_1(\nu_{as}(CH_2)_{2930}, t, T) - \mathbf{PH}_2(\nu_{as}(CH_3)_{2960}, t, T)}{\mathbf{PH}_1(\nu_{as}(CH_2)_{2930}, t, T)}$	**Hydrophilicity (Hph)** $\frac{\mathbf{PH}_1(\text{AM II}_{1550}, t, T) - \mathbf{PH}_2(\text{AM I}_{1650}, t, T)}{\mathbf{PH}_1(\text{AM II}_{1550}, t, T)}$	**Albumin (Alb)** $\frac{\mathbf{PH}_1(\delta(COO^-)_{1400}, t, T) - \mathbf{PH}_2(\delta(CH_2)_{1450}, t, T)}{\mathbf{PH}_1(\delta(COO^-)_{1400}, t, T)}$
Lactate (Lact) $\frac{\mathbf{PH}_1(\delta(C\text{–}O\text{–}H)_{1121}, t, T) - \mathbf{PH}_2(\delta(C\text{–}O\text{–}H)_{1171}, t, T)}{\mathbf{PH}_1(\delta(C\text{–}O\text{–}H)_{1121}, t, T)}$	**Glycosylation (Gly)** $\frac{\mathbf{PH}_1(\delta(C\text{–}O\text{–}H)_{1030}, t, T) - \mathbf{PH}_2(\delta(C\text{–}O\text{–}H)_{1171}, t, T)}{\mathbf{PH}_1(\delta(C\text{–}O\text{–}H)_{1030}, t, T)}$	**Hydrophobicity Index (HPI)** $\frac{\mathbf{PH}_1(\nu_{as}(CH_2)_{2930}, t, T)}{\mathbf{PH}_2(\nu_{as}(CH_3)_{2960}, t, T)}$

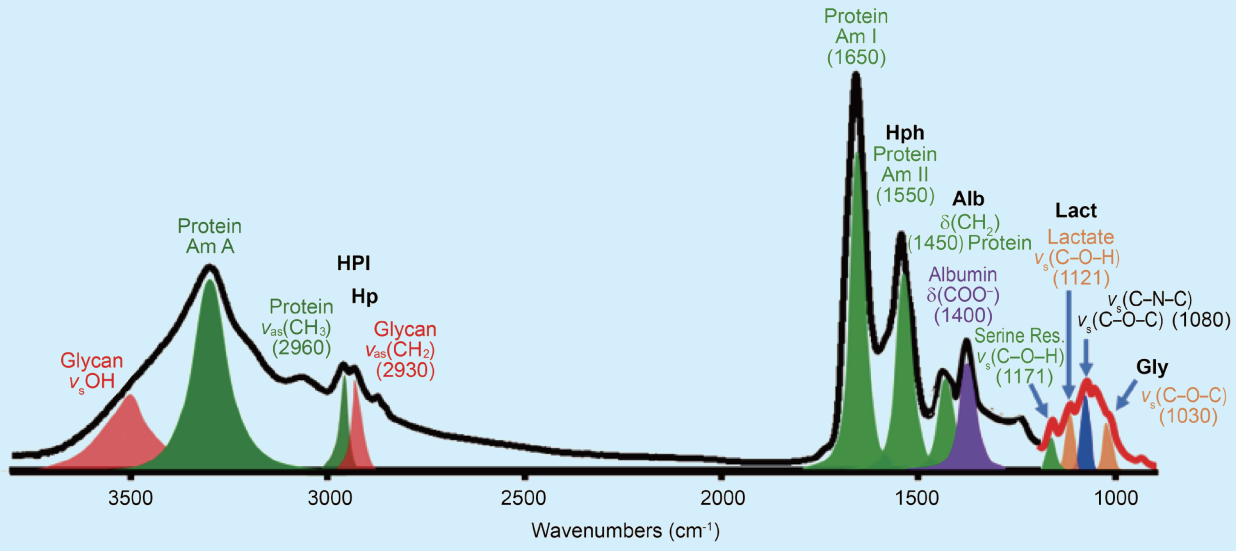

Fig. 1: The RAD equation is determined by five spectral indices (Lactate (Lact), Glycosylation (Gly), Hydrophobicity (Hp), Hydrophilicity (Hph), and Albumin (Alb)) and their respective band assignments. [Reproduced from Ref. 1]

One of the most compelling findings is that RAD gaps correlate strongly with standard clinical indicators such as serum creatinine, urine total protein, and the urine protein-to-creatinine ratio. In acute LN patients, RAD gaps for IgG glycosylation, lactate, and serum hydrophobicity increased during disease flares and decreased as treatment took effect. Conversely, the serum hydrophilicity and albumin RAD gaps displayed opposite trends, mirroring the well-known drop in serum albumin during active inflammation. Because these optical signatures respond rapidly to biochemical changes, they provide a quick, sensitive means to detect early shifts in LN status.

To consolidate all spectral information into a single, clinically relevant score, the team developed iPath software, which calculates the Prognosis Prediction Function from the five RAD gaps. This composite score closely follows patient trajectories—even over more than 700 days of follow-up—and frequently indicates improvement or relapse earlier than conventional laboratory tests. The study highlights that spectral-based indices can assist clinicians in detecting flare-ups, assessing treatment response, and tailoring immunosuppressive regimens.

In addition to IR spectroscopy, the researchers examined the structural consequences of immune activation by analyzing purified IgG samples at the **TPS 13A** biological small-angle X-ray scattering (BioSAXS) beamline. SAXS measurements revealed that IgG molecules from patients with active LN exhibited a larger radius of gyration (Rg), indicating conformational changes likely associated with altered glycosylation patterns. For example, initial samples from an acute LN patient showed Rg values around 57 Å—significantly higher than those measured after remission or in healthy controls (~50 Å). This cross-validation demonstrates a strong link between biochemical IR signatures and macromolecular structural changes, reinforcing the diagnostic value of the RAD-based approach.

The clinical implications are substantial. LN is a heterogeneous disease: two patients with similar biopsy findings may respond very differently to the same therapy. By providing rapid, quantitative, and minimally invasive biochemical readouts, this IR-based assay enables monitoring of each patient's disease status with much greater temporal resolution than current methods. Because ATR-FTIR measurements require only microliters of serum and no additional reagents, the technique is cost-effective and suitable for repeated testing—a key advantage in the long-term management of autoimmune diseases. Furthermore, the underlying principles of the method are generalizable. The RAD framework can be applied to other conditions in which serum composition reflects disease activity, such as metabolic disorders, infections, and inflammatory diseases. The integration of synchrotron IR spectroscopy, chemometric algorithms, and computational enhancement represents an emerging direction in clinical diagnostics, bridging the physics-based measurement with biomedical interpretation.

The collaboration between clinicians and synchrotron scientists demonstrates how advanced photon-based tools can address unmet medical needs. By utilizing the high brilliance and stability of the **TLS 14A1** IR beamline and validating structural signatures with the **TPS 13A** BioSAXS beamline, the team developed a multimodal platform that captures both molecular composition and macromolecular structure. This work highlights NSRRC's expanding role in translational research and precision health technologies. (Reported by Orion Shih)

*This report features the work of Mei-Ching Yu and her collaborators published in Biosensors **15**, 39 (2025).*

TPS 13A Biological Small-angle X-ray Scattering
TLS 14A1 IR Microscopy

- FTIR, SAXS
- Biomedical Science, Biophysics, Structural Biology, Analytical Chemistry

Reference

1. M.-C. Yu, X.-D. Huang, C.-W. Kuo, K.-F. Zhang, P.-C. Liang, U.-S. Jeng, P.-Y. Huang, F.W.K. Tam, Y.-C. Lee, Biosensors **15**, 39 (2025).